UC Irvine
UC Irvine Previously Published Works

Title

The Effect of Tropical Pacific Air-Sea Coupling on the Rainfall Response to Quadrupled CO2 Forcing

Permalink

https://escholarship.org/uc/item/4344h33x

Journal

Geophysical Research Letters, 50(15)

ISSN

0094-8276

Authors

Hsu, Tien-Yiao

Magnusdottir, Gudrun

Primeau, Francois

Publication Date

2023-08-16

DOI

10.1029/2023gl103466

Peer reviewed

Geophysical Research Letters®

Key Points:

- Air-sea momentum coupling enhances equatorial sea surface temperature (SST) response
- The frictional ocean flow, parallel with the surface wind stress, contributes half of the ocean heat convergence response near the equator
- The SST and vertical wind response to greenhouse gas forcing are modulated by the ocean's temperature and vertical velocity distribution

The Effect of Tropical Pacific Air-Sea Coupling on the Rainfall Response to Quadrupled CO_2 Forcing

Tien-Yiao Hsu[1] [ID]**, Gudrun Magnusdottir[2]** [ID]**, and Francois Primeau[2]** [ID]

[1]Scripps Institution of Oceanography, University of California, San Diego, La Jolla, CA, USA, [2]Department of Earth System Science, University of California, Irvine, CA, USA

Abstract We perform quadrupled CO_2 climate simulations with the Community Earth System Model version 1 (CESM1) to study how air-sea coupling affects the response of tropical rainfall under global warming. We use a hierarchy of ocean models to separate the effects of seasonal mixed-layer entrainment, wind-driven Ekman flows directed perpendicular to the wind, and the near-equator frictional flows directed in the same direction as the wind. We show that the Pacific Ocean's enhanced equatorial warming pattern (EEW) and equatorward ITCZ contraction observed in previous climate simulations emerge when the ocean model includes wind-driven Ekman and frictional flows. Furthermore, the near-equator frictional flow contributes more than half of the heat convergence in the equatorial Pacific Ocean. Finally, we show that although Ekman flow and near-equator frictional flow can both result in EEW, their coupled interactions with the Hadley circulation lead to opposite feedbacks on EEW's strength.

Plain Language Summary The ocean is important in modulating the atmospheric response to climate change. Here, we study how air-sea coupling affects the response of tropical rainfall under global warming. To identify the importance of individual ocean processes, we use a hierarchy of ocean models to separate the effects of seasonal mixed-layer entrainment, wind-driven Ekman flows, and frictional flows. We show that including Ekman and frictional flows allows our simulation to produce the Pacific Ocean's enhanced equatorial warming pattern and equatorward ITCZ contraction noted in previous climate simulations. We also show that the frictional flow, which has yet to receive much attention, is as important as the Ekman flow in generating equatorial heat convergence.

1. Introduction

Climate simulations predict that the intertropical convergence zone (ITCZ) will contract equatorward in response to global warming (e.g., Byrne & Schneider, 2016b; Lau & Kim, 2015; Zhou et al., 2019), a phenomenon known as the deep-tropical contraction. The resulting change in the pattern of tropical convection is expected to affect climate variability (Fang & Yu, 2020; Yun et al., 2021), and produce a tropical forcing that will impact the extra-tropics through atmospheric teleconnections (Alexander et al., 2002; Newman et al., 2016; Shin & Sardeshmukh, 2011). However, the predicted tropical rainfall changes are uncertain because of large differences in the response patterns produced in different climate models (Byrne et al., 2018; Long et al., 2016; Ma & Xie, 2013). Here, we present a study aiming at elucidating the role of air-sea coupling in the deep-tropical contraction phenomenon.

The deep-tropical contraction involves an increased meridional moist static energy gradient (Byrne et al., 2018; Byrne & Schneider, 2016a, 2016b; Neelin et al., 2003) coherent with the enhanced equatorial warming (EEW) of sea surface temperature (SST) (Huang et al., 2013; Zhou et al., 2019). Previous studies have identified a reduced Ekman-driven upwelling as the primary oceanic process contributing to the EEW (e.g., Chemke & Polvani, 2018; Vecchi & Soden, 2007). However, near the equator, the vanishing of the Coriolis force allows the frictional force (the force that is opposite to the wind direction) to participate in the local force balance, driving a downwind flow, the role of which in shaping the EEW has not been assessed in the literature. Here, we address this gap by clarifying the contribution of Ekman and near-equator frictional flows in driving the EEW.

We use the hierarchy of ocean models developed by Hsu et al. (2022) that can switch Ekman and frictional flows on or off while maintaining the same control climatology. We perform experiments with the hierarchy where the climate forcing is a quadrupling of atmospheric CO_2. We will show that the inclusion of Ekman and frictional flows allows the model to reproduce the equilibrium tropical response as simulated in the model coupled with

an ocean general circulation model (OGCM). Most importantly, we will show that at the equator, the warming caused by the frictional flow is comparable with the ocean warming caused by the Ekman flow.

The paper is structured as follows: In Section 2, we briefly introduce the hierarchy of ocean models, the definition of the oceanic Ekman and frictional flows, and the experimental design. In Section 3, we present the results of our experiments and we discuss the results. In Section 4, we summarize the main conclusions.

2. Methods

2.1. Hierarchy of Ocean Models Within the CESM1 Framework

The hierarchy of ocean models we use was developed in Hsu et al. (2022). It is unique in that it fits within the CESM1 framework. At the top of the hierarchy sits the Parallel Ocean Program version 2 (POP2; R. Smith et al., 2010), the full ocean global climate model within CESM1, below which we have three successively simpler ocean models: the Ekman mixed-layer model (EMOM), the mixed-layer model (MLM) and the slab ocean model (SOM). Each ocean model in the hierarchy can be substituted into the CESM framework and run coupled to the other component models of the CESM1 (e.g., the atmosphere and sea-ice models). The complete implementation details for the hierarchy are given in Section 2 of Hsu et al. (2022), and the source code of EMOM can be found at https://github.com/meteorologytoday/EMOM.

Briefly, the lowest model in the hierarchy, the SOM, has a single vertically well-mixed slab ocean with a thickness that varies horizontally but remains constant in time. The SOM does not have any entrainment or oceanic flow. The MLM further allows the mixed-layer thickness to vary temporally following a prescribed annual cycle. This allows the MLM to capture seasonal entrainment and detrainment. The EMOM then adds interactive Ekman transport to the MLM. The EMOM assigns a fixed thickness to both the Ekman transport layer and the layer representing the Ekman return flow. Finally, the POP2 is a full ocean general circulation model (OGCM) representing the most realistic ocean model of the hierarchy, and is the default ocean model in CESM1.

To maintain a similar pre-industrial (PI, see Section 2.3) climatology, it is necessary to apply unique flux corrections to the SOM, MLM, and EMOM models. These flux corrections compensate for the mean heat transport in the full OGCM (i.e., POP2) not explicitly represented in the simplified ocean models. The significant contribution to the flux corrections from the heat transport due to the Atlantic Meridional Overturning Circulation (AMOC) is of particular importance. Because we do not change the flux corrections in the PI and 4xCO2 simulations, we are effectively assuming that once equilibrium is reached, there is no appreciable change in the interhemispheric heat transport due to AMOC in response to the $4 \times CO_2$ perturbation. Section 3.1 shows that this is the case, justifying our usage of the simplified ocean models with fixed flux corrections.

2.2. Surface Flow Parameterization

The wind-driven mass transport can be separated into two components (Hsu et al., 2022):

$$\vec{M} = \vec{M}_{EK} + \vec{M}_{FR}, \tag{1}$$

with

$$\vec{M}_{EK} = \frac{f}{f^2 + \epsilon^2}(\tau^y, -\tau^x), \tag{2}$$

$$\vec{M}_{FR} = \frac{\epsilon}{f^2 + \epsilon^2}(\tau^x, \tau^y), \tag{3}$$

where $\vec{M}_{EK}$ is the Ekman mass transport, $\vec{M}_{FR}$ is the frictional mass transport, f is the Coriolis parameter, ϵ is the Rayleigh friction coefficient, and τ^x and τ^y are the zonal and meridional components of the surface wind stress. Positive values of τ^x mean that the wind is eastward and for τ^y northward. The frictional mass transport is in the same direction as the wind stress, while the Ekman mass transport is directed 90° to the right of the wind stress in the northern hemisphere and 90° to the left of the wind stress in the southern hemisphere. Provided $\epsilon \ll f$, $\vec{M}_{EK}$ approximates what is traditionally considered to be the Ekman mass transport. Note that at the equator $\vec{M}_{EK} = 0$ and $\vec{M}_{FR}$ accounts for all the mass transport. In EMOM, the mass transport is confined to the top 50 m of the

ocean. From now on, we will refer to this 50 m thick upper-most part of the water column as the Ekman layer. The parameterization used in EMOM imposes a return flow of equal magnitude in a 353.7-m-thick layer immediately below the Ekman layer. This return flow ensures that there is no mass accumulation in any water column. The frictional parameter, ϵ, is set as 1.4 day^{-1}. This value was determined by minimizing the difference between the vertical velocity in EMOM and POP2 in the top 50 m of the ocean within 10°S and 10°N in the pre-industrial run (PI, see Section 2.3 for details). This choice of ϵ implies that the frictional mass transport dominates over the Ekman mass transport in the latitude band between 5°S and 5°N (see Hsu et al., 2022).

2.3. Experimental Design

We conducted two sets of experiments. The first set consists of pre-industrial (PI) control runs in which the CO_2 volume mixing ratio is kept constant at 284.7 ppm. For the simulations using the SOM, MLM, and EMOM ocean models we did 200-year-long runs. Equilibrium was reached after 100 years. For the simulation using POP2, we used a 1,000-year-long uncoupled ocean-only spin-up run available from NCAR as the initial condition and then did an additional 200-year-long coupled simulation. In all cases, we use the last 30 years to represent the equilibrium climatology.

In the second set of experiments, we abruptly quadrupled atmospheric CO_2 and then kept it constant at 1138.8 ppm. For the simulation using the SOM ocean model, we did a 200-year-long run. For the simulations using the MLM and EMOM ocean models, we did 300-year-long runs, and for the POP2 case we did a 700-year-long run. In all cases, we used the last 30 years to represent the new equilibrium climate.

3. Results

3.1. Approach to Equilibrium in the Quadrupled CO_2 Experiment

The abrupt increase in atmospheric CO_2 in the $4 \times CO_2$ experiments leads to an adjustment process toward a new equilibrium. To briefly characterize the adjustment, we show the time evolution of the mean SST in each hemisphere in Figures 1a and 1b. The SOM (blue) takes less than 50 years to reach equilibrium as its ocean has the least mass. The MLM (orange) and EMOM (green) take about 200 years to reach equilibrium because the temporal variation of the mixed layer thickness increases the effective mass of water interacting with the atmosphere. POP2 takes approximately 500 years to reach a new quasi-equilibrium (red). Its adjustment involves fluctuations that appear closely related to changes in the strength of the AMOC. The time evolution of AMOC strength, defined as the maximum value of the Atlantic overturning stream function north of 20°N and below the depth of 500 m, is shown in Figure 1e. The cross-equatorial ocean heat transport (OHT) in the Atlantic is shown in Figure 1f. Figure 1g shows the mean AMOC stream function for PI (in black contours), and for $4 \times CO_2$ averaged over years 671–700 (in green contours). The shading shows the difference in stream function over the last 30 years (671–700 of $4 \times CO_2$ minus 171–200 of PI).

It is also important to examine the evolution of sea ice in POP2 because its variability is associated with freshwater perturbations that strongly affect AMOC (Sévellec et al., 2017; R. Smith & Gregory, 2009; Zhang & Delworth, 2005). The decrease in sea-ice volume (Figures 1c and 1d) means that freshwater is released into the ocean, resulting in the weakening of the AMOC (Figure 1e). After year 500, the evolution of mean SST, total sea-ice volume, and AMOC (Figures 1a–1f) flatten, meaning the system reaches a new quasi-equilibrium in which there is a shoaling of the lower limb of the overturning circulation (Figure 1g).

Since the difference of cross-equatorial AMOC OHT between the final and the beginning stage of the simulation is small, there is a window of opportunity for applying the EMOM ocean hierarchy that assumes no change in AMOC OHT, that is, with the flux correction kept fixed in the PI and $4 \times CO_2$.

3.2. Equilibrium Tropical Response in the Pacific Ocean

The tropical response is shown in Figure 2. In the SST plot, we subtract the mean SST anomaly in the tropics to study the spatial pattern of anomalous SST response.

In EMOM, the magnitude of increased rainfall is similar to that of POP2 while the peak of the anomalous rainfall in EMOM is centered more equatorward than in the POP2 simulation. This suggests that the increased rainfall due to momentum coupling may be largely attributed to the oceanic Ekman response. In later paragraphs, we will
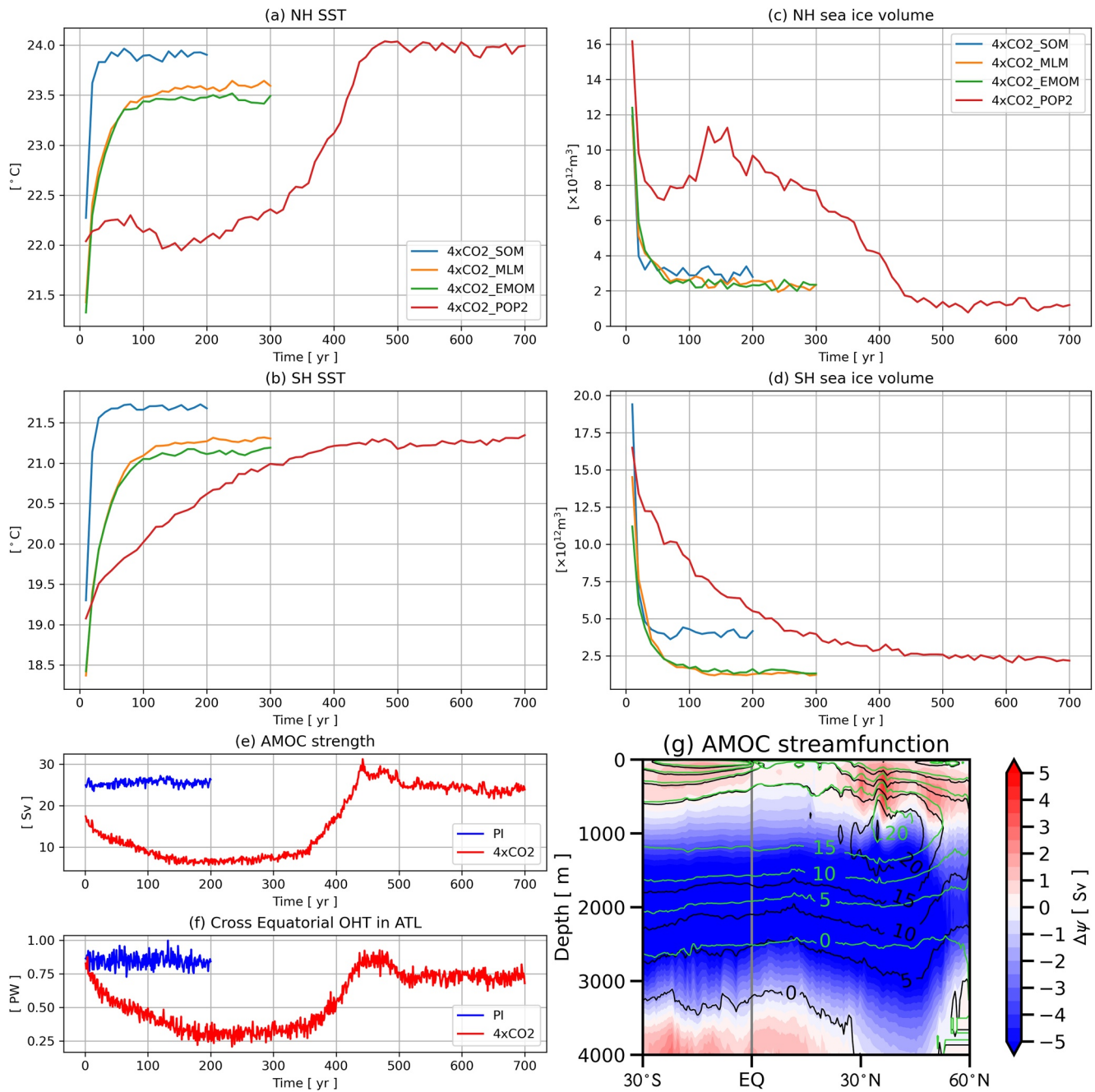
Figure 1. (a–f) time evolution of the globally integrated quantities for the forced simulation in the model hierarchy. (a) and (b): the mean sea-surface temperatures (SSTs) of the northern and southern hemispheres, respectively. (c) and (d): the total sea-ice volumes in the northern and southern hemispheres, respectively. (e): the strength of Atlantic meridional overturning circulation (AMOC) in POP2. The strength of AMOC is defined as the maximum value of the streamfunction of AMOC north of 20°N and below the depth of 500 m. The blue curve represents the simulation of the pre-industrial control run (PI), the red represents the simulation of the run of quadruple CO_2 (4 × CO_2). (f): the ocean heat transport (OHT) on the equator in the Atlantic Ocean. Color coding is the same (e). (g): the AMOC streamfunction for PI (black contours) and 4 × CO_2 (green contours) in depth-latitude space. The shading is the difference in the mean streamfunction averaged over the last 30 years of each simulation, that is, 4 × CO_2 (year 671–700) minus PI (year 171–200).

argue that the details of the simulated Ekman flow are important in producing the correct location of the peak anomalous rainfall.

In POP2, the anomalous SST has a meridional cold-warm-cold tripole pattern, that is, an EEW pattern, with the warm anomalous SST along the equator in the Eastern Pacific. EMOM produces a similar enhanced tropi-
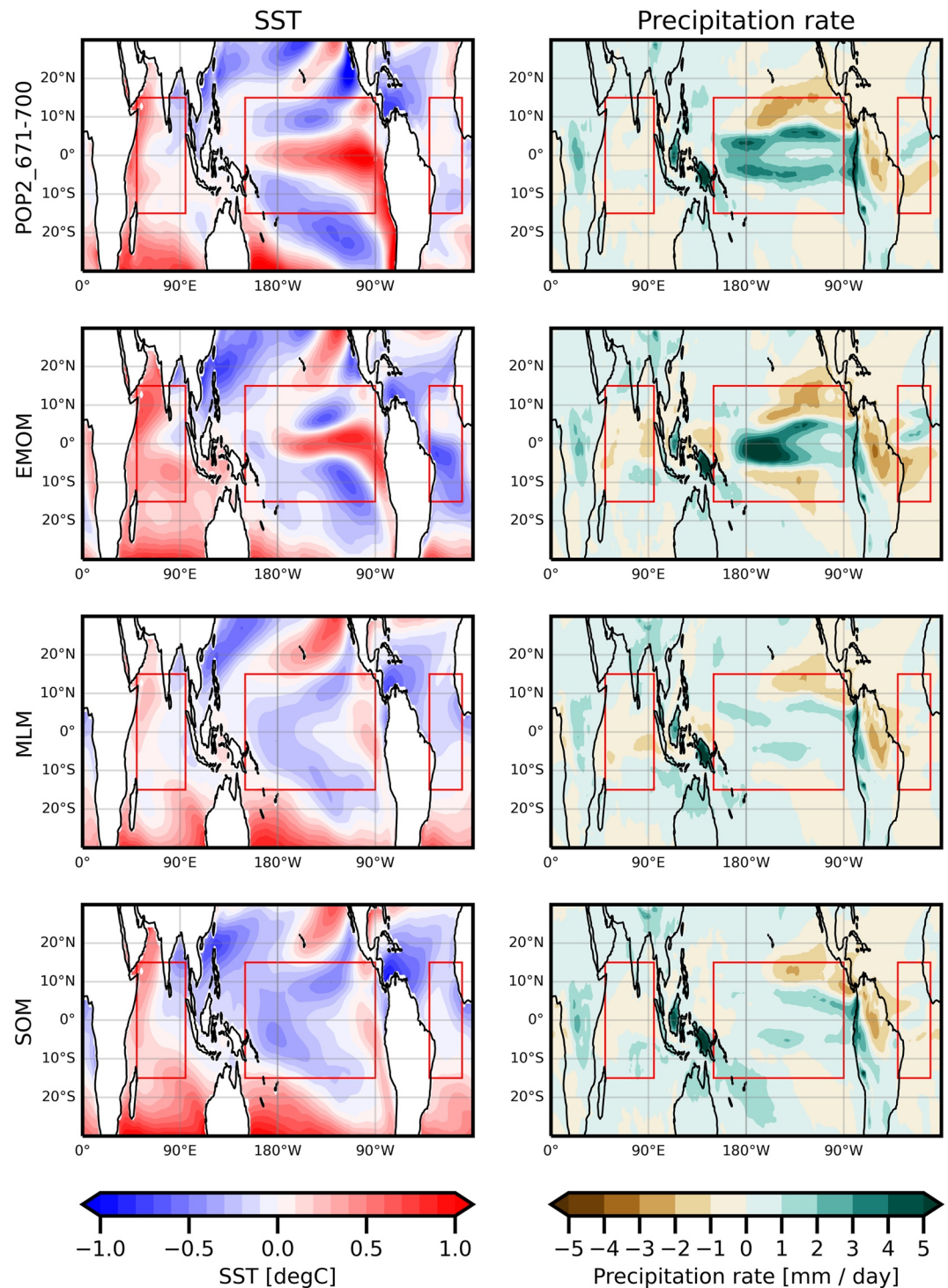
Figure 2. The response of forced simulation for each hierarchy member. The left column shows the response in sea-surface temperature (SST). The tropical mean SST (30°S–30°N) is subtracted to show the pattern. The right column shows the response in the annual mean precipitation rate. The ocean domains boxed in red will be used to compute the zonal mean quantities in Figures 3 and 4, Figures S1 and S2 in Supporting Information S1.

cal rainfall and SST tripole pattern. The enhanced rainfall and the SST tripole pattern in EMOM are squeezed equatorward compared to POP2. There is also a dry response at the southern flank of the ITCZ in EMOM that is absent in POP2. In the SOM and MLM, there is a weak strengthening of the ITCZ and the EEW pattern is missing because of the absence of the equatorial warm tongue.
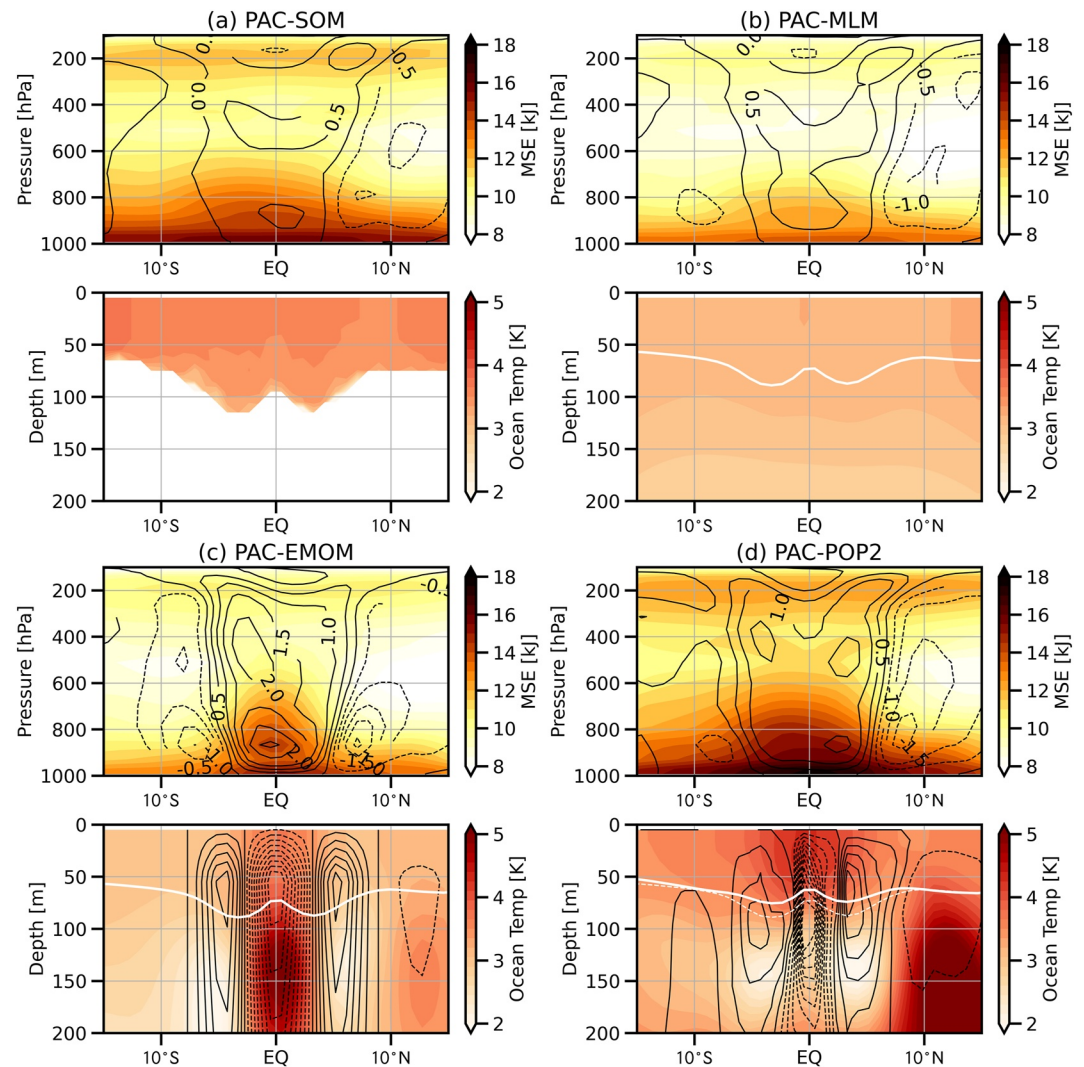
Figure 3. The response in the atmosphere and ocean for the forced simulation ($4 \times CO_2$) in each hierarchy member over Pacific Ocean. (a): SOM, (b): MLM, (c): EMOM, and (d) POP2. For each pair of panels, the top panel shows the response of the atmospheric moist static energy (shading) and the vertical velocity, $-\omega$, with contours in the unit Pa/s. Notice that we plot negative ω so that positive values imply ascending air motion. The contour interval is 0.5 Pa/s. Each bottom panel shows the response in ocean temperature (shading) and vertical velocity w (contours) with contour interval of 10 m/yr. The white solid and dashed curve is the annual mean mixed-layer thicknesses in the pre-industrial control run (PI) and $4 \times CO_2$ run, respectively.

The atmospheric response is tightly connected to the meridional SST response. Figure 3 shows the zonal mean response over the Pacific for both the atmosphere (moist static energy kJ as shading, vertical velocity Pa/s as contours) and the ocean (temperature K as shading, and vertical velocity m/s as contours) in each hierarchy member. In general, all models produce enhanced ascending air motions at the equator and descending air motions off the equator (8°S and 8°N). The descending air motions are stronger in the northern hemisphere.

The changes in the tropical mean SST and the meridional SST gradient between the equatorial and off-equatorial regions are both important in driving the atmospheric response of vertical air motion. Warmer mean SST enhances moist static energy in the atmosphere, resulting in stronger latent heat release and therefore stronger upward motion. A stronger meridional SST gradient between the equatorial and off-equatorial regions produces relative air motion, that is, upward on the equator and downward off the equator, which increases the meridional gradient of latent heat release and then strengthens the meridional circulation in between (consistent with the enhanced surface meridional wind stress response in Figure 4c). As seen in Figure 3, the SOM and MLM
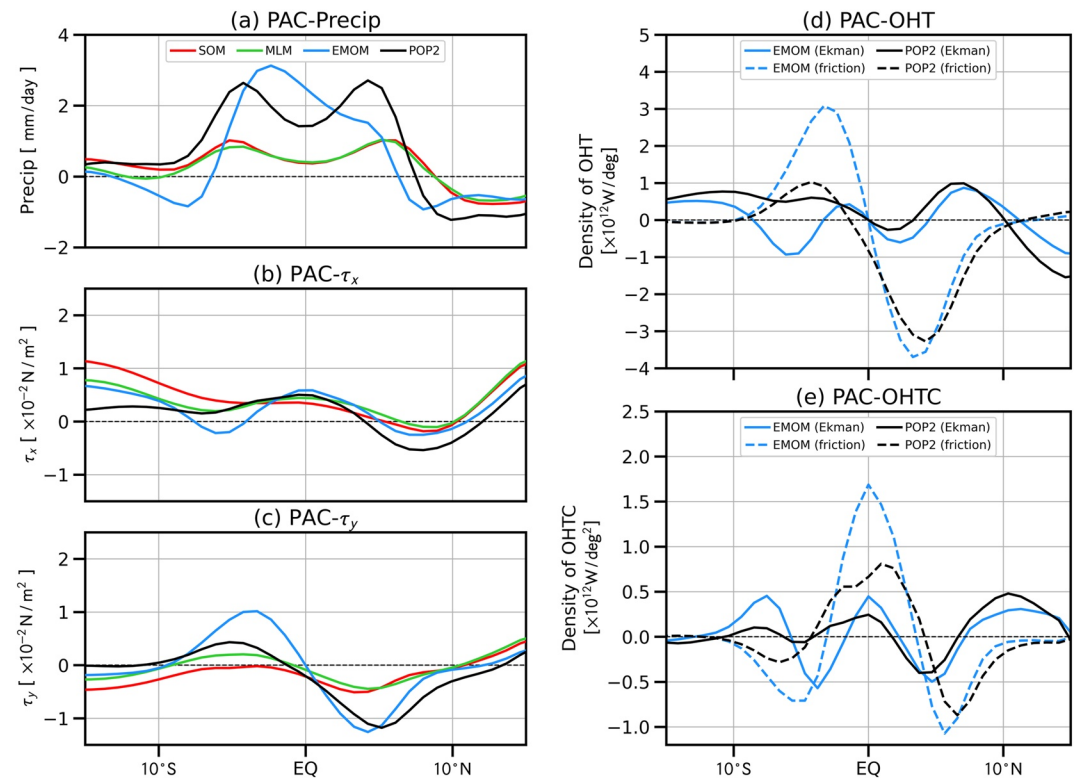
Figure 4. The atmospheric and oceanic response of hierarchy members in the forced simulation in the Pacific Ocean. (a): the response in zonal-mean, annual-mean precipitation. (b): the response in zonal-mean, zonal-wind stress at the surface with positive values indicating that the anomalous wind is blowing eastward. (c): the response of the zonal mean meridional wind stress on the sea surface with positive values meaning the anomalous wind is blowing northward. (d): the response of ocean heat transport (OHT) density. (e): the response of OHT convergence (OHTC) density. The density of OHT and OHTC means the OHT and OHTC per degree longitude. For the calculation of OHT please see Supplementary Information.

have uniform increases in temperature at the equator. The increased SST in the $4 \times CO_2$ experiment leads to an increase in atmospheric ascent by 0.5 Pa/s. In EMOM and POP2, the ascent rate increases are considerably greater (3.0 and 1.5 Pa/s, respectively) because of the higher mean SST and the greater meridional SST gradient. The stronger ascent carries anomalous moisture into the air to generate stronger moist static energy anomalies in the mid-troposphere in EMOM and POP2 compared to MLM and SOM. This inter-hierarchy comparison demonstrates that the mean increase in SST and the increase in SST gradient are both important.

The mean SST response is related to the mixed-layer-induced entrainment. This is best elaborated on by comparing the SOM (Figure 3a) and MLM (Figure 3b) results. Because the heat in the mixed layer of the MLM simulation is transported downward via seasonal entrainment, the simulated SST in the MLM is about 0.5°C cooler than in the SOM simulation. The resulting heat anomaly below the mixed layer is slowly attenuated by the weak temperature restoring term in the model formulation (Hsu et al., 2022).

The response of meridional SST gradients is related to the asymmetric depth of maximum ocean upwelling. In the EMOM simulations (Figure 3c), vertical motions reach their maxima at a depth of 50 m. This depth is effectively prescribed by the choice of a 50-m-thick Ekman layer in the model. It is also shallower than the annual mean mixed-layer depth (white solid line). For POP2 (Figure 3d), the upwelling maximum in the northern hemisphere is at the depth of 60 m, which is within the mixed-layer depth (white solid and dashed lines), and the upwelling maximum in the southern hemisphere is at 110 m, which is deeper than the mixed layer. Therefore, the asymmetric upwelling depth in POP2 creates asymmetric SST cooling and hence asymmetric meridional SST gradient response.

Processes other than Ekman transport also influence the tropical SST. For example, the equatorial downwelling in the POP2 simulation does not create as strong a warm anomaly as in EMOM because the subducted heat in POP2

is transported poleward through processes absent in EMOM. This poleward heat transport eventually upwells so that the heating anomaly acts to reduce the efficiency with which off-equator upwelling cools the surface. The result is a weaker SST gradient response in POP2 compared to EMOM, and a stronger overall SST warming. The unresolved processes might also contribute to the strong Central Pacific atmospheric ascent in EMOM compared to POP2 (Figure S1 in Supporting Information S1), and may further impact other basins through an anomalous Walker circulation.

While the effect of the Ekman flow has been discussed in the literature (e.g., Chemke & Polvani, 2018; Vecchi & Soden, 2007), the result of the frictional flow that acts in the same direction as the wind has not been discussed in the literature. The anomalous zonal and meridional wind stress contributes to the oceanic vertical motion. The anomalously weakened trade winds over the equator (Figure 4b) generate the equatorial downwelling through the convergent Ekman flow. Similarly, the anomalously convergent meridional wind (Figure 4c) induces convergent frictional flow in the ocean that contributes to additional equatorial downwelling.

The decomposition of OHT and OHT convergence (OHTC) in POP2 and EMOM provides more information about the relative importance of Ekman and frictional flow in the SST response. Figures 4d and 4e show the OHT and OHTC in the Pacific tropics (see Supplementary Information on how we compute OHT). The OHT response for EMOM and POP2 is similar in the northern hemisphere. In the southern hemisphere, the strong subsidence discussed earlier slightly strengthens the trade winds (Figure 4b), and produces an anomalous southward OHT. It is important to note that the frictionally-driven OHT and its convergence are equal to or stronger than those due to the Ekman flow in the Pacific Ocean. Similar behavior is found in the Atlantic and Indian Oceans (see supplementary Figures S2a–S2i and Figures S3a–S3i in Supporting Information S1). Therefore, the role of the frictional flow cannot be neglected in the analysis of the equatorial SST response.

3.3. The Role of the Frictional Flow

The past literature has revealed the role of the Ekman flow in enhancing convection along the equator through the weakening of the trade winds (e.g., Chemke & Polvani, 2018; Vecchi & Soden, 2007). However, we also find that the contribution of warming due to the convergent frictional flow is equally important and sometimes contributes more than that of the Ekman flow in the Pacific.

Another important aspect is that although the contributions of Ekman and frictional flows are of the same sign in our simulations, their interactions with SST will result in opposite feedbacks. If there is an anomalous equatorial SST, the stronger meridional SST gradient will drive a stronger Hadley cell. The intensified Hadley cell implies stronger trade winds that decrease the equatorial SST by inducing Ekman pumping that upwells the cold subsurface water. This causality implies a negative feedback of equatorial SST through the Ekman flow. Oppositely, if there is an anomalous equatorial SST, the strengthened Hadley cell will lead to stronger convergence of meridional wind at the equator. The convergent meridional wind will drive convergent frictional flows that increase the equatorial SST by reducing the equatorial upwelling, and thus the SST warms further. This causality implies a positive feedback of equatorial SST through the frictional flow. Therefore, we believe that correctly identifying the Ekman and frictional flows in climate models will help us understand the SST response in the tropical oceans.

4. Conclusion

Understanding the mechanisms that modulate the response of tropical convection in response to global warming will help reduce uncertainties in climate models. Since oceanic Ekman flow dominates the tropical OHT (Klinger & Marotzke, 2000), the air-sea Ekman coupling is invoked to explain the role of ocean modulation. In this study, we performed $4 \times CO_2$ coupled climate simulations using an ocean model hierarchy to isolate the effect of Ekman coupling on tropical rainfall. This is made possible because there is no substantial change in the AMOC-driven meridional heat transport once the system reaches its new equilibrium. This allows us to use the ocean hierarchy that assumes no change in AMOC.

We find that Ekman flow coupling amplifies the rainfall response. The heat transport analysis shows that both the Ekman and the frictional flow induce OHT. The contribution of the frictionally induced OHT dominates the one caused by the Ekman flow. The frictional and Ekman flow modulation of the SST response is sensitive to the structure of the associated overturning circulation and the subsurface diffusive processes. The unresolved

subsurface heat transport changes the final meridional SST gradient, which is important to tropical circulations. In this study, we are not addressing what contributes to the asymmetry of vertical motions in the simulation of POP2. Still, it is an important feature of our simulation, and more work should be done to understand its physical origin. We note that the result in EMOM depends on the choice for the Rayleigh friction coefficient ϵ, and the choice of the Ekman layer depth. These deserved more attention in future studies.

Given the importance of the frictional flow, more work is required to identify the frictional flow in observational data and OGCM output. While some pioneering work has been done in understanding Ekman transport at the equator (Cronin & Kessler, 2009), the frictional flow was not their focus. Moreover, there should be more research on various aspects of frictional flow and its impact on climate dynamics, such as its influence on the variability of tropical rainfall, and even on the modeled precipitation biases found in different climate models.

Data Availability Statement

The code and data used to produce the paper figures are publicly available at https://doi.org/10.5281/zenodo.7678955 and https://doi.org/10.5281/zenodo.7677817.

References

Alexander, M. A., Bladé, I., Newman, M., Lanzante, J. R., Lau, N.-C., & Scott, J. D. (2002). The atmospheric bridge: The influence of ENSO teleconnections on air–sea interaction over the global oceans. *Journal of Climate*, *15*(16), 2205–2231. https://doi.org/10.1175/1520-0442(2002)015<2205:tabtio>2.0.co;2

Byrne, M. P., Pendergrass, A. G., Rapp, A. D., & Wodzicki, K. R. (2018). Response of the intertropical convergence zone to climate change: Location, width, and strength. *Current Climate Change Reports*, *4*(4), 355–370. https://doi.org/10.1007/s40641-018-0110-5

Byrne, M. P., & Schneider, T. (2016a). Energetic constraints on the width of the intertropical convergence zone. *Journal of Climate*, *29*(13), 4709–4721. https://doi.org/10.1175/jcli-d-15-0767.1

Byrne, M. P., & Schneider, T. (2016b). Narrowing of the ITCZ in a warming climate: Physical mechanisms. *Geophysical Research Letters*, *43*(21), 11–350. https://doi.org/10.1002/2016gl070396

Chemke, R., & Polvani, L. (2018). Ocean circulation reduces the Hadley cell response to increased greenhouse gases. *Geophysical Research Letters*, *45*(17), 9197–9205. https://doi.org/10.1029/2018gl079070

Cronin, M. F., & Kessler, W. S. (2009). Near-surface shear flow in the tropical Pacific cold tongue front. *Journal of Physical Oceanography*, *39*(5), 1200–1215. https://doi.org/10.1175/2008jpo4064.1

Fang, S.-W., & Yu, J.-Y. (2020). A control of ENSO transition complexity by tropical Pacific mean SSTS through tropical-subtropical interaction. *Geophysical Research Letters*, *47*(12), e2020GL087933. https://doi.org/10.1029/2020gl087933

Hsu, T.-Y., Primeau, F., & Magnusdottir, G. (2022). A hierarchy of global ocean models coupled to CESM1. *Journal of Advances in Modeling Earth Systems*, *14*(8), e2021MS002979. https://doi.org/10.1029/2021ms002979

Huang, P., Xie, S.-P., Hu, K., Huang, G., & Huang, R. (2013). Patterns of the seasonal response of tropical rainfall to global warming. *Nature Geoscience*, *6*(5), 357–361. https://doi.org/10.1038/ngeo1792

Klinger, B. A., & Marotzke, J. (2000). Meridional heat transport by the subtropical cell. *Journal of Physical Oceanography*, *30*(4), 696–705. https://doi.org/10.1175/1520-0485(2000)030<0696:mhtbts>2.0.co;2

Lau, W. K., & Kim, K.-M. (2015). Robust Hadley circulation changes and increasing global dryness due to CO_2 warming from CMIP5 model projections. *Proceedings of the National Academy of Sciences*, *112*(12), 3630–3635. https://doi.org/10.1073/pnas.1418682112

Long, S.-M., Xie, S.-P., & Liu, W. (2016). Uncertainty in tropical rainfall projections: Atmospheric circulation effect and the ocean coupling. *Journal of Climate*, *29*(7), 2671–2687. https://doi.org/10.1175/jcli-d-15-0601.1

Ma, J., & Xie, S.-P. (2013). Regional patterns of sea surface temperature change: A source of uncertainty in future projections of precipitation and atmospheric circulation. *Journal of Climate*, *26*(8), 2482–2501. https://doi.org/10.1175/jcli-d-12-00283.1

Neelin, J., Chou, C., & Su, H. (2003). Tropical drought regions in global warming and El Niño teleconnections. *Geophysical Research Letters*, *30*(24). https://doi.org/10.1029/2003gl018625

Newman, M., Alexander, M. A., Ault, T. R., Cobb, K. M., Deser, C., Di Lorenzo, E., et al. (2016). The Pacific decadal oscillation, revisited. *Journal of Climate*, *29*(12), 4399–4427. https://doi.org/10.1175/jcli-d-15-0508.1

Sévellec, F., Fedorov, A. V., & Liu, W. (2017). Arctic sea-ice decline weakens the Atlantic meridional overturning circulation. *Nature Climate Change*, *7*(8), 604–610. https://doi.org/10.1038/nclimate3353

Shin, S.-I., & Sardeshmukh, P. D. (2011). Critical influence of the pattern of tropical ocean warming on remote climate trends. *Climate Dynamics*, *36*(7), 1577–1591. https://doi.org/10.1007/s00382-009-0732-3

Smith, R., Jones, P., Briegleb, B., Bryan, F., Danabasoglu, G., Dennis, J., et al. (2010). The Parallel Ocean Program (POP) reference manual: Ocean component of the Community Climate System Model (CCSM) and Community Earth System Model (CESM). LAUR-01853, *141*, 1–140.

Smith, R. S., & Gregory, J. M. (2009). A study of the sensitivity of ocean overturning circulation and climate to freshwater input in different regions of the North Atlantic. *Geophysical Research Letters*, *36*(15). https://doi.org/10.1029/2009gl038607

Vecchi, G. A., & Soden, B. J. (2007). Global warming and the weakening of the tropical circulation. *Journal of Climate*, *20*(17), 4316–4340. https://doi.org/10.1175/jcli4258.1

Yun, K.-S., Lee, J.-Y., Timmermann, A., Stein, K., Stuecker, M. F., Fyfe, J. C., & Chung, E.-S. (2021). Increasing ENSO–rainfall variability due to changes in future tropical temperature–rainfall relationship. *Communications Earth & Environment*, *2*(1), 1–7. https://doi.org/10.1038/s43247-021-00108-8

Zhang, R., & Delworth, T. L. (2005). Simulated tropical response to a substantial weakening of the Atlantic thermohaline circulation. *Journal of Climate*, *18*(12), 1853–1860. https://doi.org/10.1175/jcli3460.1

Zhou, W., Xie, S.-P., & Yang, D. (2019). Enhanced equatorial warming causes deep-tropical contraction and subtropical monsoon shift. *Nature Climate Change*, *9*(11), 834–839. https://doi.org/10.1038/s41558-019-0603-9